



SAKARYA ÜNİVERSİTESİ

FEN BİLİMLERİ ENSTİTÜSÜ DERGİSİ

Sakarya University Journal of Science
SAUJS

ISSN 1301-4048 e-ISSN 2147-835X Period Bimonthly Founded 1997 Publisher Sakarya University
<http://www.saujs.sakarya.edu.tr/>

Title: Position Estimation of In-Pipe Robot using Artificial Neural Network and Sensor Fusion

Authors: Abdullah Erhan AKKAYA, Muhammed Fatih TALU, Ömür AYDOĞMUŞ

Received: 2021-03-16 16:46:59

Accepted: 2021-06-09 00:00:00

Article Type: Research Article

Volume: 25

Issue: 5

Month: October

Year: 2021

Pages: 1102-1120

How to cite

Abdullah Erhan AKKAYA, Muhammed Fatih TALU, Ömür AYDOĞMUŞ; (2021), Position Estimation of In-Pipe Robot using Artificial Neural Network and Sensor Fusion.

Sakarya University Journal of Science, 25(5), 1102-1120, DOI:

10.16984/saufenbilder.898072

Access link

<http://www.saujs.sakarya.edu.tr/en/pub/issue/65589/898072>

New submission to SAUJS

<http://dergipark.gov.tr/journal/1115/submission/start>

Position Estimation of In-Pipe Robot Using Artificial Neural Network and Sensor Fusion

Abdullah Erhan AKKAYA^{*1}, Muhammed Fatih TALU¹, Ömür AYDOĞMUŞ²

Abstract

Automatic position detection of water leakage in water distribution pipelines is critical to minimize the loss of labour, time, money spent on exploration and excavation in pipe inspection procedures. Nevertheless, the main goal of detection is to prevent water loss. In this paper, accurate position detection, crack frequency band detection, and external sphere studies of an in-pipe robot prototype were presented. During the precise position estimation, classical Extended Kalman Filter (EKF), stationary region detection, and location estimation using Enhanced Heuristic Drift Elimination (EHDE) were performed with two different artificial neural networks (ANNs). In this way, online precise position estimation can be done on hardware with no sufficient computational power for indoor robotic studies. In addition, the sound characteristics resulting from the crack at different hole size and water pressure intensity levels were investigated. Finally, a new sealing sphere design was devised. Three different hydrophone sensor data were recorded on the SD card simultaneously. The results show that the proposed ANN method can work online and make a similar position estimation with the classical IMU position estimation method by 99%.

Keywords: Sensor Fusion, Artificial Neural Network, Inertial Navigation, Leak Detection

* Corresponding author: erhan.akkaya@inonu.edu.tr

¹ Inonu University, Faculty of Engineering, Department of Computer Engineering, Malatya, Turkey.

E-Mail: erhan.akkaya@inonu.edu.tr; fatihtalu@gmail.com.

ORCID: <https://orcid.org/0000-0001-6193-5166>; <https://orcid.org/0000-0003-1166-8404>.

² Firat University, Faculty of Technology, Department of Mechatronic Engineering, Elazig, Turkey.

E-Mail: oaydogmus@firat.edu.tr.

ORCID: <https://orcid.org/0000-0001-8142-1146>.

1. INTRODUCTION

Water has great importance for the survival of living beings on earth and especially for the human species. Increasing the place of settlements in proportion to the human population also increases the water demand. Today's people should consume water cost-effectively for future generations to benefit from potable water resources. In many countries, serious policies have been developed, including water distribution systems for the conscious use of water [1]. According to World Bank, approximately 14.6 billion dollars of water is lost annually due to the cracks in the water pipes during transportation [2]. In another report prepared by the World Bank, two-thirds of the world's population will be going without water in 2025 unless the current water policies are taken under control [3]. In the U.S., approximately 240,000 water pipe cracks occur annually. These cracks are responsible for the loss of 2 trillion gallons of water that account for 15-25% of purified water [4].

One way of protecting water is by reducing water losses due to pipe cracks and faults in the pipelines in the distribution network. These faults should be identified and repaired to prevent loss of water and income. General pipe repairs have high costs in distribution networks. Finding the exact position of the fault and working in that area reduces the repair costs. Although surface pipe listening devices appear to be a solution to this need, they are not preferred because of influenced by external noise [5]. Moreover, the small scale of underground water leaks makes it very difficult to detect these leaks. Physical infrastructure failures, such as ageing, corrosion and mechanical stress, cause the water pipe to lose its thickness what causes cracking and water leakage due to pipe leaks/breaks [6]. Pipe maintenance must be carried out regularly to prevent damage. Traditional maintenance procedures have high costs as they require removal and excavation. Comprehensive pipe maintenance procedures include; (a) the detection of the amount of water lost in the pipes; (b) finding the location of the cracks in the pipeline that causing water loss; (c) the repair of the cracked areas in the detected position [7]. The amount of lost water is

determined by calculating the difference between the amount of water supplied to the grid and the amount used [8].

In the literature, there are many studies on distribution water leak detection and management. In monitoring and managing physical losses, various methods have been applied, such as the implementation of standard water balance and performance monitoring [9]–[12], monitoring of minimum night flow, determination of potentially preventable leaks daily [13], [14], implementation of pressure management [15], [16], pipe material management [17]–[19], in-pipe location detection robots that can find leak position [20]–[23]. In this preliminary study, a leak detection robot prototype, which can find the position of the pipe crack with high accuracy, was developed.

2. PRECISE POSITION ESTIMATION EXPERIMENTS

The operations were performed in the precise position estimation step are summarized as follows: (1) saving IMU data in navigation scenarios, (2) position estimation method, (3) Kuka experiments, (4) proposed artificial position estimation method.

2.1. Saving IMU Data in Navigation Scenarios

Navigation scenarios were carried out in a 20m² indoor space. There are eight different navigation scenarios, as shown in Figure 1. For the real-time recording of IMU data during navigation, Odroid XU3 and IMU sensor were connected. This navigation device was placed in a sphere-shaped housing produced by a 3D printer. IMU data was recorded between the nodes in the scenarios with the help of the navigation device. Figure 2 shows the navigation device and indoor space. An IMU that has nine degrees of freedom was used to collect the data. These nine degrees consists of a 3DOF accelerometer, 3DOF magnetometer and 3DOF gyroscope. The sensor data was read at 100Hz from the IMU sensor using virtual port listening software written in C++. The read data was transferred to the Odroid XU3 computer via

a USB port. Figure 3 shows the recorded IMU data for the navigation scenario.

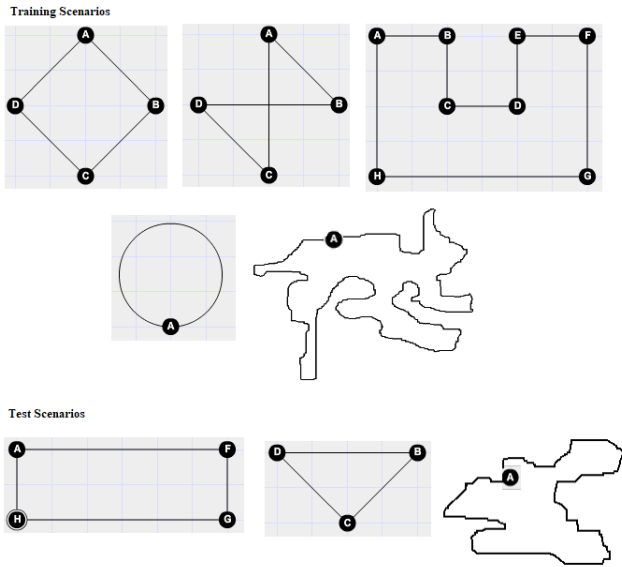


Figure 1 Navigation scenarios



Figure 2 Obtaining train and test data via IMU sensor that placed in 3D printed spherical ball

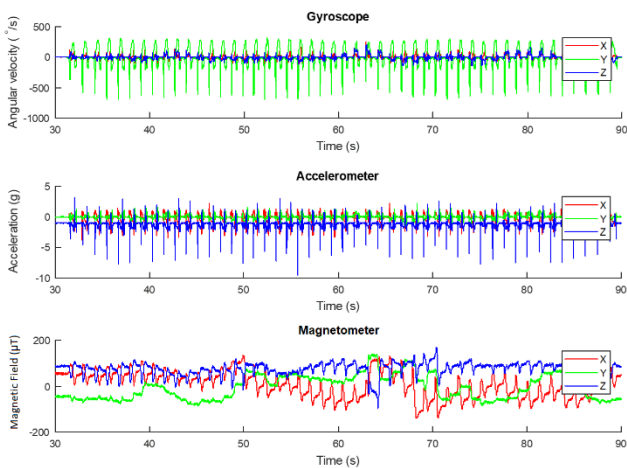


Figure 3 IMU data for a square navigation scenario

2.2. Position Estimation Method

Combining the data obtained from different sensors such as magnetometers, accelerometers, and gyroscopes, obtaining the measurement information with the smallest error is called sensor fusion [24]. The direct processing of raw IMU data results in an increase in cumulative error in the acceleration sensor data required for calculating the position, thereby decreasing position estimation accuracy. Therefore, data need to be filtered. Kalman filter has been used effectively in sensor fusion applications [25]–[28]. Rudolf Kalman, an American citizen of Hungarian origin, discovered The Kalman filter in 1960 [29]. First developed for linear systems, Kalman Filter is a recursive, least-squares algorithm in which weights are dynamically updated at each step. The Extended Kalman Filter (EKF) aims to apply the Kalman filter to a non-linear system [30].

In general, the Kalman filter is a filter that can predict the state of the system at the time $t-1$ using the input and output information of a dynamic system. Kalman Filter is defined in Equation (1) and (2) [31]. At Equation (1), x represents the state vector, u control vector, w process noise, A state transition matrix, B control input matrix. The z value in Equation (2) represents the measurement vector, H the transformation matrix that maps the state vector parameters to the measurement region, and v represents the measurement noise.

$$x_t = A_t x_{t-1} + B_t u_t + w_t \tag{1}$$

$$z_t = H_t x_t + v_t \tag{2}$$

The state dynamics are not linear in many systems. In this case, the Kalman filter cannot be applied because the Kalman gain cannot be calculated. The standard Kalman filter has been used by calculating the Jacobian values of the functions to linearize the system’s state dynamics and measurement function. Initially, the system state dynamics are linearized, followed by the measurement (system dynamics) update in the following step. In the third step, measurements are linearized, and the last step is updated. As a

result of this process, the Kalman filter transforms to the Extended Kalman Filter [30]. In the first step, the linearized state and measurement vectors are given in Equations (3) - (4).

$$x_{t+1} = f(x_t, u_t, w_t) \quad (3)$$

$$z_t = h(x_t, u_t, v_t) \quad (4)$$

The basic steps of the Extended Kalman Filter are listed below.

Step 1: Linearize measurements

$$H_t = \left. \frac{\partial h(x,u)}{\partial x} \right|_{x=\hat{x}_{t|t-1}} \quad (5)$$

Step 2: Update measurements (correction):

$$K_t = P_{t|t-1} H_t^T (H_t P_{t|t-1} H_t^T + R_t)^{-1} \quad (6)$$

$$\hat{x}_{t|t} = \hat{x}_{t|t-1} + K_t (z_t - H_t \hat{x}_{t|t-1}) \quad (7)$$

$$P_{t|t} = P_{t|t-1} - K_t H_t P_{t|t-1} \quad (8)$$

Step 3: Update measurements (correction):

$$F_t = \left. \frac{\partial f(x,u)}{\partial x} \right|_{x=\hat{x}_{t|t}} \quad (9)$$

Step 4: Time update (prediction) and return step1:

$$\hat{x}_{t+1|t} = f(\hat{x}_{t|t}, \hat{u}_t) \quad (10)$$

$$P_{t+1|t} = F_t P_{t|t} F_t^T + Q_t \quad (11)$$

In this study, 3DOF magnetic field sensor and 3DOF accelerometer sensors were used as complementary sensors [32]. A sensor fusion process was performed to correct the angular variation measured by a 3DOF gyroscope in the method used in leak detection. The integration step is the time update step which predicts the quaternion vector using the F_t transition matrix and the estimated error covariance matrix. The vector observation step optimizes the system state dynamics of the magnetic field sensor and the accelerometer data. The Kalman filter was applied at the final stage to minimize the error covariance, and the correction step is done. The noise characteristics of the sensors (acceleration,

rotation and magnetic field) were calculated by taking the mean and standard deviations of the data collected while the IMU was inactive [20].

The state vector of the generated filter system is defined in Equation (12). q_0 is the real component, q_1 , q_2 , and q_3 are the virtual components of the quaternion vector.

$$x = [q_0 \quad q_1 \quad q_2 \quad q_3] \quad (12)$$

Euler angles have been calculated by passing the IMU data through the Extended Kalman Filter in classical studies. Since the rotation vector calculated by the Euler angle has the singularity problem, Quaternion vector q was calculated instead of the Euler angles. The following steps show the implementation of the Kalman Filter.

2.2.1. Integration Step

The gyroscope sensor measures the angular change in the X, Y and Z axes of the coordinate system in rad/s, the change in each axis is represented by ω_x , ω_y , ω_z , respectively. ${}^S\omega$ represents the gyroscope vector measured in all axes of the sensor coordinate system, eq. (13).

Equation (14) was used to calculate the quaternion derivative (${}^S\dot{q}$) which gives the amount of change from the global coordinate system to the sensor coordinate system [33].

$${}^S\omega = [0 \quad \omega_x \quad \omega_y \quad \omega_z] \quad (13)$$

$${}^S\dot{q} = \frac{1}{2} {}^S\hat{q} \otimes {}^S\omega \quad (14)$$

The quaternion derivative was calculated by multiplying the values read from the gyroscope sensor sequentially given in Equation (15). ${}^S\omega_t$ represents the data read from the gyroscope at time t , ${}^S\hat{q}_{est,t-1}$ represents the previous quaternion vector. After these derivatives have added to the previous quaternion by multiplying by the sensor period Δt the quaternion, the orientation information has been obtained in Equation (16) [32].

$${}^S_G\dot{q}_{\omega,t} = \frac{1}{2} {}^S_G\hat{q}_{est,t-1} \otimes {}^S\omega_t \quad (15)$$

$${}^S_Gq_{\omega,t} = {}^S_G\dot{q}_{\omega,t}\Delta t + {}^S_G\hat{q}_{est,t-1} \quad (16)$$

Assume that the sensor operates at a frequency of 50Hz. In this case, Δt period value will be 0.02. In every 0.02 seconds, the current quaternion vector was multiplied by the gyroscope value ${}^S\omega_t$ from the sensor to obtain the instant quaternion value. The effect of the calculated quaternion value on a total period of 1 second is 0,02. The quaternion was multiplied by this value and collected with the vector calculated in the previous step. As shown in Figure 4, the initial quaternion $[1 \ 0 \ 0 \ 0]$ was rotated 90 degrees on the X-axis.

When the gyroscope process noise has added to the state equation, the general state equation of the system given in (17). The w_t value is the process noise defined by the covariance matrix Q of the gyroscope sensor [32].

$$x_t = f(x_{t-1}) + w_t \quad (17)$$

In principle, the Q covariance matrix and w_t are the same. The formulation is represented by the w_t in the optimization formulas and Q by the Kalman filter. Q covariance matrix is different even for the same brand sensor. When a sensor is stationary, it produces values unequal to zero due to external noise. After reading all these values for a certain period, the sensor's offset value was calculated by taking the arithmetic mean of the sensor data, Equation (18). In this paper, the offset value of the gyroscope sensor was added to the variance estimation algorithm. The variance vector of the sensor was calculated in (19). The variance vector Q is used in the construction of the covariance matrix.

$$offset = [[-0.1342 \ -0.0553 \ 0.1455]] \quad (18)$$

$$var = [0.0705 \ 0.0732 \ 0.0663] \quad (19)$$

When ${}^S_G\dot{q}_{\omega,t}$ is replaced by Equation (15) in Equation(16), main quaternion equation is obtained [16], Equation (20).

$${}^S_Gq_{\omega,t} = \frac{1}{2} ({}^S_G\hat{q}_{est,t-1} \otimes {}^S\omega_t)\Delta t + {}^S_G\hat{q}_{est,t-1} \quad (20)$$

This equation which is estimated, is defined as the state equation in the Kalman filter. The x_t was calculated at the time t is also the predicted ${}^S_G\hat{q}_{est,t-1}$ value in the previous step. When all these equations are combined, a Kalman filter state equation based on quaternion is defined in Equation (21). The state equation at time t is given in Equation (22).

$$f(x_{t-1}) = \frac{1}{2} (x_{t-1} \otimes {}^S\omega_t)\Delta t + x_{t-1} \quad (21)$$

$$x_{t|t-1} = f(x_{t-1|t-1}) \quad (22)$$

It is clear that the function $f(x_t)$ is not linear. In this case, since the Kalman Filter cannot calculate the Kalman gain, F_t transition matrix should be computed using the Extended Kalman Filter. After $x_{t-1} \otimes {}^S\omega_t$ quaternion production, Equation (23) is obtained [32].

$$x_{t-1} \otimes {}^S\omega_t = \begin{bmatrix} x_0 \cdot 0 - x_1\omega_x - x_2\omega_y - x_3\omega_z \\ x_0\omega_x + x_1 \cdot 0 + x_2\omega_z - x_3\omega_y \\ x_0\omega_y - x_1\omega_z + x_2 \cdot 0 + x_3\omega_x \\ x_0\omega_z + x_1\omega_y - x_2\omega_x + x_3 \cdot 0 \end{bmatrix} \quad (23)$$

In Equation (24), The Jacobian F_t transition matrix of the $f(x_{t-1})$ function obtained when Equation (23) is replaced in Equation (21).

$$F_t = \left. \frac{\partial f(x_t)}{\partial x} \right|_{x=\hat{x}_{t-1|t-1}} = \begin{bmatrix} 1 & -\Delta t/2 \cdot \omega_x & -\Delta t/2 \cdot \omega_y & -\Delta t/2 \cdot \omega_z \\ \Delta t/2 \cdot \omega_x & 1 & \Delta t/2 \cdot \omega_z & -\Delta t/2 \cdot \omega_y \\ \Delta t/2 \cdot \omega_y & -\Delta t/2 \cdot \omega_z & 1 & \Delta t/2 \cdot \omega_x \\ \Delta t/2 \cdot \omega_z & \Delta t/2 \cdot \omega_y & -\Delta t/2 \cdot \omega_x & 1 \end{bmatrix} \quad (24)$$

The estimated quaternion vector is obtained by multiplying the initial quaternion value by F_t , in Equation (25).

$$x_{t|t-1} = F_t x_{t-1|t-1} \quad (25)$$

The final step of the integration step is the calculation of the estimated covariance matrix ($P_{t|t-1}$) according to Equation (11) in the fourth step of the EKF.

2.2.2. Vector observation step

The observation step is the step in which the quaternion vector is optimized using auxiliary sensors. As a result of the optimization, the minimized quaternion, z_t observation vector was obtained. ${}^S_G\hat{q}$, ${}^G\hat{d}$ and ${}^S\hat{s}$ represents the sensor orientation, the predefined reference direction on the earth, the data read from the sensor, respectively. The objective function to be minimized is defined by (26) [32].

$$\begin{aligned} \min_{{}^S_G\hat{q}} f({}^S_G\hat{q}, {}^G\hat{d}, {}^S\hat{s}) &\rightarrow f({}^S_G\hat{q}, {}^G\hat{d}, {}^S\hat{s}) \\ &= {}^S_G\hat{q}^* \otimes {}^G\hat{d} \otimes {}^S_G\hat{q} - {}^S\hat{s} \end{aligned} \quad (26)$$

Using the Gradient Descent method, the quaternion equation to be solved with μ step size and the Jacobian matrix of the function indicating the direction of the error are given in the (27) and (28), respectively. The ∇ symbol indicates that the objective function is solved by the Gradient Descent method [32].

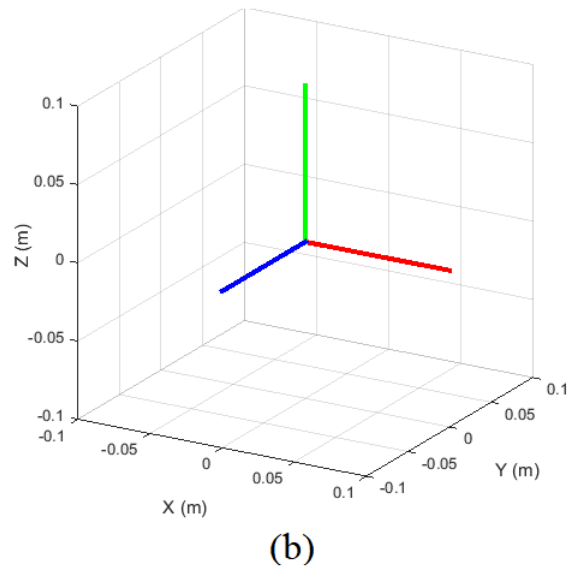
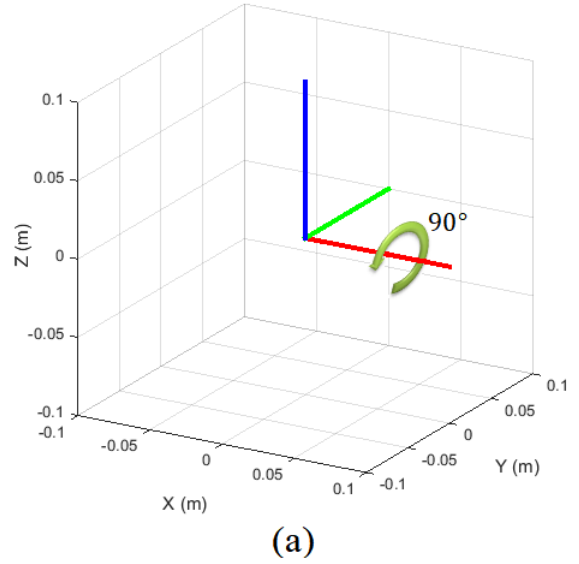


Figure 2 Rotating the IMU sensor around X-axis.

$${}^S_G\hat{q}_{k+1} = {}^S_G\hat{q}_k - \mu \frac{\nabla f({}^S_G\hat{q}_k, {}^G\hat{d}, {}^S\hat{s})}{\|\nabla f({}^S_G\hat{q}_k, {}^G\hat{d}, {}^S\hat{s})\|} \quad (27)$$

$$\nabla f({}^S_G\hat{q}_k, {}^G\hat{d}, {}^S\hat{s}) = J^T({}^S_G\hat{q}_k, {}^G\hat{d}) f({}^S_G\hat{q}_k, {}^G\hat{d}, {}^S\hat{s}) \quad (28)$$

The quaternion vector provides the coordinate transformation to be used in the calculations given in Equation (29). Given that the gravitational vector in the global coordinate system defines the Z-axis of the invariant gravity vector, the model refers to the angular change between the information coming from the accelerometer and

the gravity vector. In this case, the reference system defined as ${}^G\hat{\mathbf{a}}$ in the objective function will be updated as ${}^G\hat{\mathbf{g}}$. The upper symbol defines the global coordinate system and $\hat{\mathbf{g}}$ defines the gravity in Equation (30). If the accelerometer is to be used only in the quaternion update, ${}^S\hat{\mathbf{a}}$ in Equation (28), the objective function of the optimization system to be installed according to Equation (26) and the Jacobian matrix are given in Equations (32) and (33). The orientation quaternion was calculated only by the accelerometer and gyroscope data [32]. This set of equations defines the Z-axis of the reference global coordinate system.

$${}^S\hat{\mathbf{q}} = [q_0 \quad q_1 \quad q_2 \quad q_3] \quad (29)$$

$${}^G\hat{\mathbf{g}} = [0 \quad 0 \quad 0 \quad 1] \quad (30)$$

$${}^S\hat{\mathbf{a}} = [0 \quad a_x \quad a_y \quad a_z] \quad (31)$$

$$f_g({}^S\hat{\mathbf{q}}, {}^S\hat{\mathbf{a}}) = \begin{bmatrix} 2(q_1q_3 - q_0q_2) - a_x \\ 2(q_0q_1 + q_2q_3) - a_y \\ 2\left(\frac{1}{2} - q_1^2 - q_2^2\right) - a_z \end{bmatrix} \quad (32)$$

$$J_g({}^S\hat{\mathbf{q}}) = \begin{bmatrix} -2q_2 & 2q_3 & -2q_0 & 2q_1 \\ 2q_1 & 2q_0 & 2q_3 & 2q_2 \\ 0 & -4q_1 & -4q_2 & 0 \end{bmatrix} \quad (33)$$

The quaternion vector calculated by the accelerometer only corrects the angle between the gravity vector, thus preventing angular orientation information from being updated in all three axes. In addition to gravity, when the magnetic axes present in the horizontal and vertical directions that define the X and Y axes of the global coordinate system are used, three orthogonal axes will be formed. Thus, three-dimensional angular orientation information was computed effectively. Equation (34) and (35) show that referenced magnetic field coordinate axes, ${}^G\hat{\mathbf{b}}$ and magnetic field sensor data, ${}^S\hat{\mathbf{m}}$, respectively.

$${}^G\hat{\mathbf{b}} = [0 \quad b_x \quad 0 \quad b_z] \quad (34)$$

$${}^S\hat{\mathbf{m}} = [0 \quad m_x \quad m_y \quad m_z] \quad (35)$$

Magnetic field sensors can produce erroneous results influenced by all the magnetic field disturbers in the external environment, such as magnets and electrical appliances [34]. These waves, which have a disturbing effect around the sensor, have been described as *hard iron bias* [35]. The sensor must be calibrated to minimize ambient noise and increase the effectiveness of the magnetic field sensor output. In this calibration process, the quaternion multiplication between the predicted quaternion value and the data read from the sensor was performed, and the magnetic field direction ${}^G\hat{\mathbf{h}}$ was measured (36). In the next step, the calibration of the reference magnetic field ${}^G\hat{\mathbf{b}}$ of the algorithm was performed, (37). Thus, it was ensured that the error is limited only by the predicted quaternion orientation and does not spread to the whole system [36].

$${}^G\hat{\mathbf{h}}_t = [0 \quad h_x \quad h_y \quad h_z] = {}^S\hat{\mathbf{q}}_{est,t-1} \otimes {}^S\mathbf{m}_t \otimes {}^S\hat{\mathbf{q}}_{est,t-1}^* \quad (36)$$

$${}^G\hat{\mathbf{b}}_t = [0 \quad \sqrt{h_x^2 + h_y^2} \quad 0 \quad h_z] \quad (37)$$

The second cost function defines the X-Y axes of the global coordinate system, and the Jacobian matrix of this function is shown in Equations (38) and (39).

$$f_b({}^S\hat{\mathbf{q}}, {}^G\hat{\mathbf{b}}, {}^S\hat{\mathbf{m}}) = \quad (38)$$

$$\begin{bmatrix} 2b_x(0.5 - q_2^2 - q_3^2) + 2b_z(q_1q_3 - q_0q_2) - m_x \\ 2b_x(q_1q_2 - q_0q_3) + 2b_z(q_0q_1 + q_2q_3) - m_y \\ 2b_x(q_0q_2 + q_1q_3) + 2b_z(0.5 - q_1^2 - q_2^2) - m_z \end{bmatrix}$$

$$J_b({}^S\hat{\mathbf{q}}, {}^G\hat{\mathbf{b}}) = \begin{bmatrix} -2b_zq_2 & 2b_zq_3 \\ -2b_xq_3 + 2b_zq_1 & 2b_xq_2 + 2b_zq_0 \\ 2b_xq_2 & 2b_xq_3 - 4b_zq_1 \\ -4b_xq_2 - 2b_zq_0 & -4b_xq_3 + 2b_zq_1 \\ 2b_xq_1 + 2b_zq_3 & -2b_xq_0 + 2b_zq_2 \\ 2b_xq_0 - 4b_zq_2 & 2b_xq_1 \end{bmatrix} \quad (39)$$

The angular change values are calculated according to gravity, or magnetic axes alone do not give the orientation information of the sensor. A single solution surface must be formed by combining the objective functions defined by equations (32) and (38). Equations (40) and (41) combines objective functions and Jacobian matrices.

$$f_{g,b}({}^S\hat{q}, {}^S\hat{a}, {}^G\hat{b}, {}^S\hat{m}) = \begin{bmatrix} f_g({}^S\hat{q}, {}^S\hat{a}) \\ f_b({}^S\hat{q}, {}^G\hat{b}, {}^S\hat{m}) \end{bmatrix} \quad (40)$$

$$J_{g,b}({}^S\hat{q}, {}^G\hat{b}) = \begin{bmatrix} J_g^T({}^S\hat{q}) \\ J_b^T({}^S\hat{q}, {}^G\hat{b}) \end{bmatrix} \quad (41)$$

Once the equation systems to be optimized was defined, the sensor function to be used was selected in Equation (42). The quaternion value

was optimized for all three axes in the next step, and the vector observation step is completed in Equation (43). The μ value is the step size, in Equation (44). The z_t measurement to be used in the next step was calculated by the observation vector in Equation (45).

H represents the observability matrix, and v_t represents observation noise. The H matrix is the unit matrix, $I_{4 \times 4}$, because of containing the z_t quaternion information.

$$\nabla f = \begin{cases} J_g^T({}^S\hat{q}_{est,t-1}) \cdot f_g({}^S\hat{q}_{est,t-1}, {}^S\hat{a}_t) \\ J_{g,b}^T({}^S\hat{q}_{est,t-1}, {}^G\hat{b}) \cdot f_{g,b}({}^S\hat{q}_{est,t-1}, {}^S\hat{a}_t, {}^G\hat{b}, {}^S\hat{m}_t) \end{cases} \quad (42)$$

$${}^S q_{\nabla,t} = {}^S\hat{q}_{est,t-1} - \mu_t \frac{\nabla f}{\|\nabla f\|} \quad (43)$$

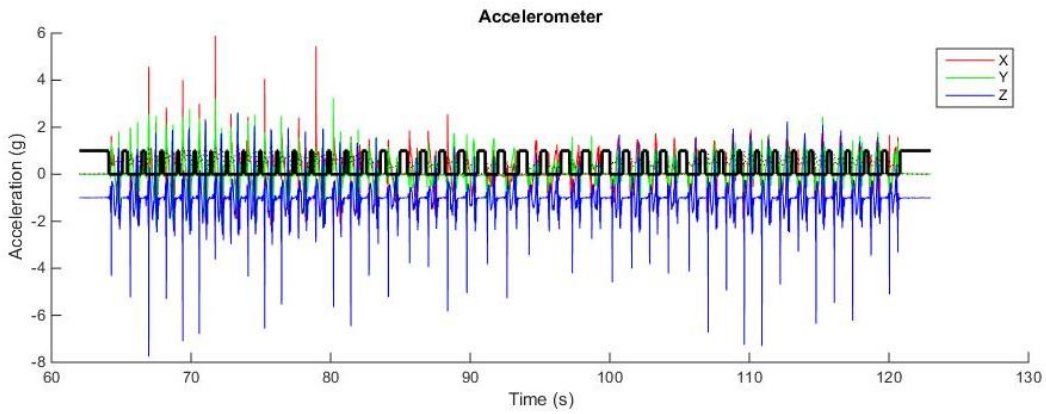


Figure 3 Determining the stationary region of the accelerometer using the Butterworth filter IMU data for a square navigation scenario

$$\mu_t = \alpha \left\| \frac{{}^S\dot{q}_{\omega,t}}{E} \right\| \Delta t, \quad \alpha > 1 \quad (44)$$

$$z_t = Hx_t + v_t = \frac{{}^S q_{\nabla,t}}{\|{}^S q_{\nabla,t}\|} \quad (45)$$

2.2.3. Kalman Filtering Step

Once the integration and vector observation steps are completed, the Kalman Filtering step starts. In this step, the Kalman gain was calculated using the estimated covariance matrix calculated in the integration step, the H observability matrix, and the R covariance matrix, Equation (46). The state correction and covariance matrix correction were performed with the calculated Kalman gain in Equations (47) and (48).

$$K_t = P_{t|t-1} H_t^T (H_t P_{t|t-1} H_t^T + R_t)^{-1} \quad (46)$$

$$\hat{x}_{t|t} = \hat{x}_{t|t-1} + K_t (z_t - H_t \hat{x}_{t|t-1}),$$

$${}^S\hat{q}_{est,t} = \hat{x}_{t|t} \quad (47)$$

$$P_{t|t} = P_{t|t-1} - K_t H_t P_{t|t-1} \quad (48)$$

The next step is the integration step. Estimated covariance matrix and estimated status update were performed. In the second stage, the z_t measurement vector was calculated using the Gradient Descent algorithm, and the Kalman filter was applied. The sensor fusion process ends after the vector observation step. Quaternion data were computed using an accelerometer, gyroscope and magnetic field sensors. The quaternion obtained

in the next step was used to compute the position. In order to be able to calculate the position correctly, it is necessary to eliminate the error in the accelerometer after calculating the quaternion vector by the sensor fusion process. First, using the quaternion values, the accelerometer values in the sensor coordinate system must be converted to the earth coordinate system [32], Equation (49).

$${}^G\hat{a} = ({}^S_G\hat{q} \otimes [0 \ a_x \ a_y \ a_z]) \otimes \hat{q}^* \quad (49)$$

After this process, the Butterworth filter was applied to the accelerometer data to determine the

sensor's fixed points and minimize the position offset. The Butterworth filter was preferred because it has a more linear frequency response than Chebyshev and the elliptical filters. Figure 5 shows the accelerometer data applied to the Butterworth filter. In the filter indicated by black, the regions with 0 value show the moving parts, and the regions with value 1 display the stationary areas. After determining the stationary regions, the velocity was calculated by integrating the accelerometer value in non-stationary regions.

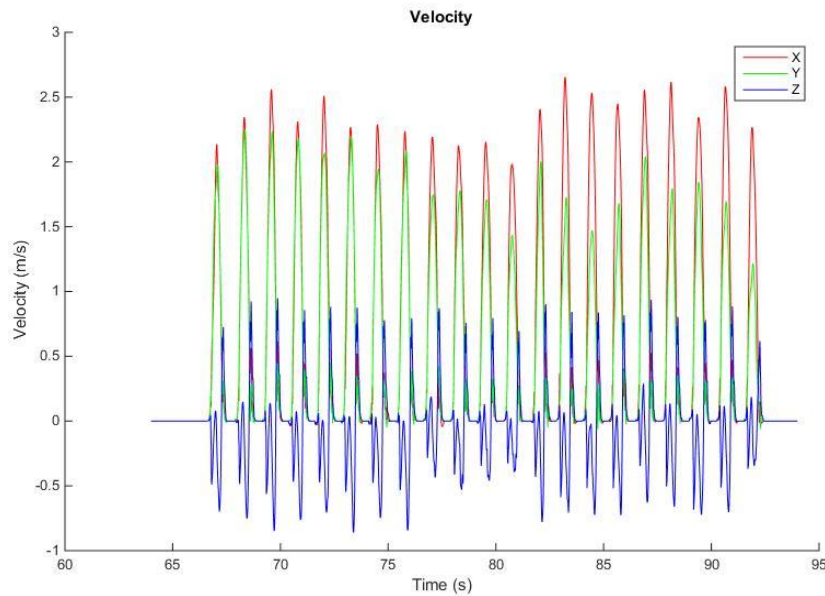


Figure 4 Sensor velocity graph resulting from the integration of accelerometer after a minute.

The calculated speed value was integrated into non-stationary regions, and the position information was calculated. The computed velocity is given in Figure 6.

2.2.4. Enhanced Heuristic Drift Elimination (EHDE)

In the fourth and last stage, the first integral of the acceleration gives the sensor speed vector, and the second integral provides the position with information. For the square navigation data, the position graph obtained at the end of the four stages is shown in Figure 7a. Although the start and endpoint of the navigation are the same, the prediction error is high. Appear of this high error

is due to the cumulative growth of the error at each step. EHDE [37] method was used to reduce the cumulative error. This method filters the deviations in the sensor orientation. For this, a curve model is inserted into the last five measurement data and calculates the dominant sensor orientation. It then minimizes the error by subtracting the orientation difference between the model and the measurement from the current Quaternion vector. When we use EHDE in square navigation data, it is seen that the prediction error between the start and end points has dropped to 0.3m (see Figure 7b). This result is sufficient to continue the design.

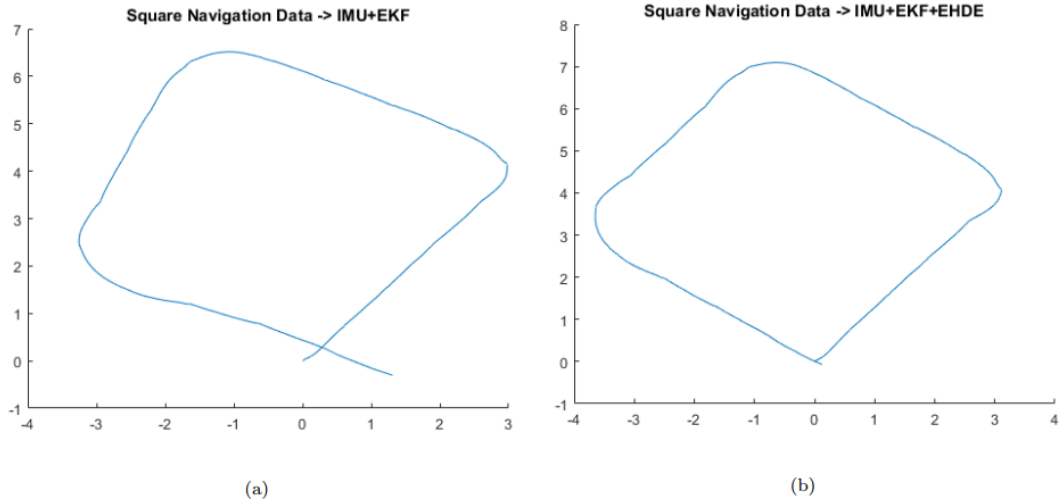


Figure 5 Position estimation results for square navigation data (a) IMU+EKF, (b) IMU + EKF + EHD



Figure 6 Experimental setup for simultaneous recording of Kuka and IMU data.

2.3. Kuka Experiments

In order to obtain the training set using Kuka Robot and IMU data, the simultaneous recording apparatus shown in Figure 8 was established. An artificial intelligence system was built to map the IMU sensor data using the precise position information obtained from the Kuka robot.

The components used in the recording device and numbered with yellow labels are listed below.

1. Software that records the XYZ position information of the robot end (JAVA)
2. Software that records the first IMU sensor data (C++)
3. Software that records the second IMU sensor data (C++)

4. Two IMU sensors placed at the end of the robot
5. Kuka robot controller
6. A computer that records the IMU and Kuka data synchronously.

Before the experiment, the Kuka robot movements were programmed by the operator using the control software interface and placed in the Kuka robot memory. In addition, both IMU sensors are fixed to the end of the Kuka. Necessary connections have been made for the flow of information from Kuka and IMUs to the computer. After the essential C++ and Java compilers were installed on the Ubuntu operating system, simultaneous data was recorded from the IMU sensors and the Kuka robot. The movements placed in the memory of the Kuka were performed at three different speeds, and during the arm

movements, Kuka/IMU data were recorded simultaneously (Figure 9a). Input and output data were trained using ANN, and the matching accuracy reached $R = 0.902$ (see Figure 9b). Although this value seems acceptable, the accumulation of the error value of 0.098 in each measurement step results in unacceptable position estimation. For this reason, different methods were researched to make position estimation more accurate, and thus artificial location estimation method was applied.

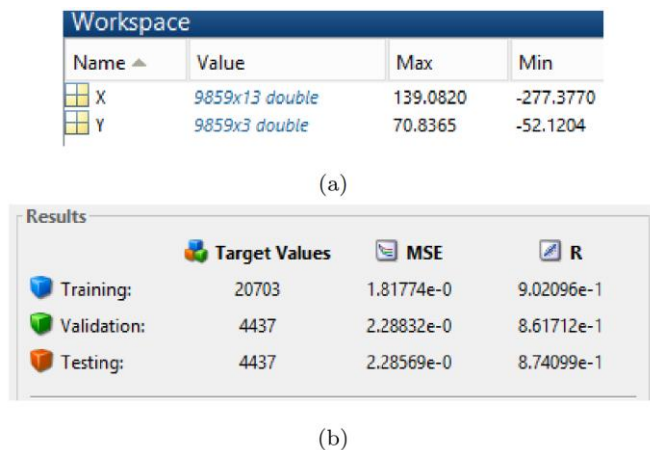


Figure 7 (a) Training data (X: input, Y: output);
(b) Training results of Kuka data.

2.4. Proposed Artificial Position Estimation Method

In the proposed artificial position estimation method, two different artificial neural networks were created which mimic the classical position estimation. The first artificial neural network input and output consists of IMU sensor data and quaternion vectors, respectively.

The input of the second ANN is the quaternion vector, and the output is position information corrected by the EHDE algorithm. Thus, it is unnecessary to know the noise characteristics of the gyroscope, accelerometer and magnetometer sensors, the mathematical background required for EKF and EHDE, and Quaternion transformations for position estimation. The ANN directly converts the IMU sensor information to position information.

The first ANN is in the NARX architecture and has 4 cells in the input layer, 18 cells in the intermediate layer, and 4 cells in the output layer. System inputs and outputs are 9DOF IMU and 4D Quaternion data, respectively. The training, validation and test accuracy obtained from the training process is approximately 99.99% (see Figure 10).

Figure 11 shows classical and artificial methods that were used to estimate quaternion from the square navigation data. The 4D-Quaternion data are shown separately.

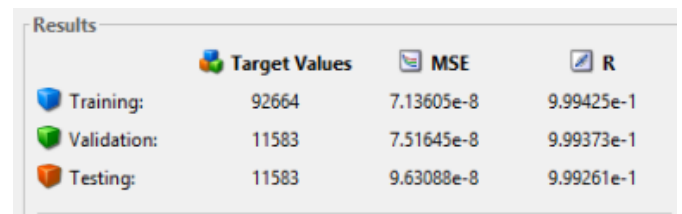


Figure 8 Training results of first ANN

It is seen that the artificial learning method produces almost the same results as the classical system has high accuracy.

Using the second ANN, the stationary zone detection and the noise elimination process performed by the EHDE method were imitated. Thus, IMU data was mapped to direct position information with two different ANNs. The fact that the location prediction process can be performed by an ANN method means that the network values can be transferred to an embedded system, and the position estimation can be run online. In this way, the online precision position estimation can be done in robotic studies (especially in the building) without sufficient speed and calculation power. Figure 12 shows the classical and recommended method results of eight different navigation positions. Since the results of two consecutive ANNs are the same as 99% of the classical method, the results are almost overlapping, as shown.

3. DETECTION OF LEAKAGE SOUND FREQUENCY BAND

The material type of the water pipe, the size of the crack and the severity of the water pressure causes

the sound from the pipe crack to be in different frequency bands. This experiment aims to examine the effect of crack hole diameter and pressure intensity on the frequency band and amplitude.

3.1. Preparing the Experiment Mechanism

Below are the different types of materials were used for the water pipe, the different sizes that the

crack may be and the different water pressure intensity values formed in the pipe.

Material Types: PCCP, RCCP, AC, PVC, HDPE, GRP, Steel, Cast Iron

Hole sizes: 2mm, 4mm, 6mm, 8mm

Water pressure intensity: 1bar, 2bar, 3bar, 4bar, 5bar

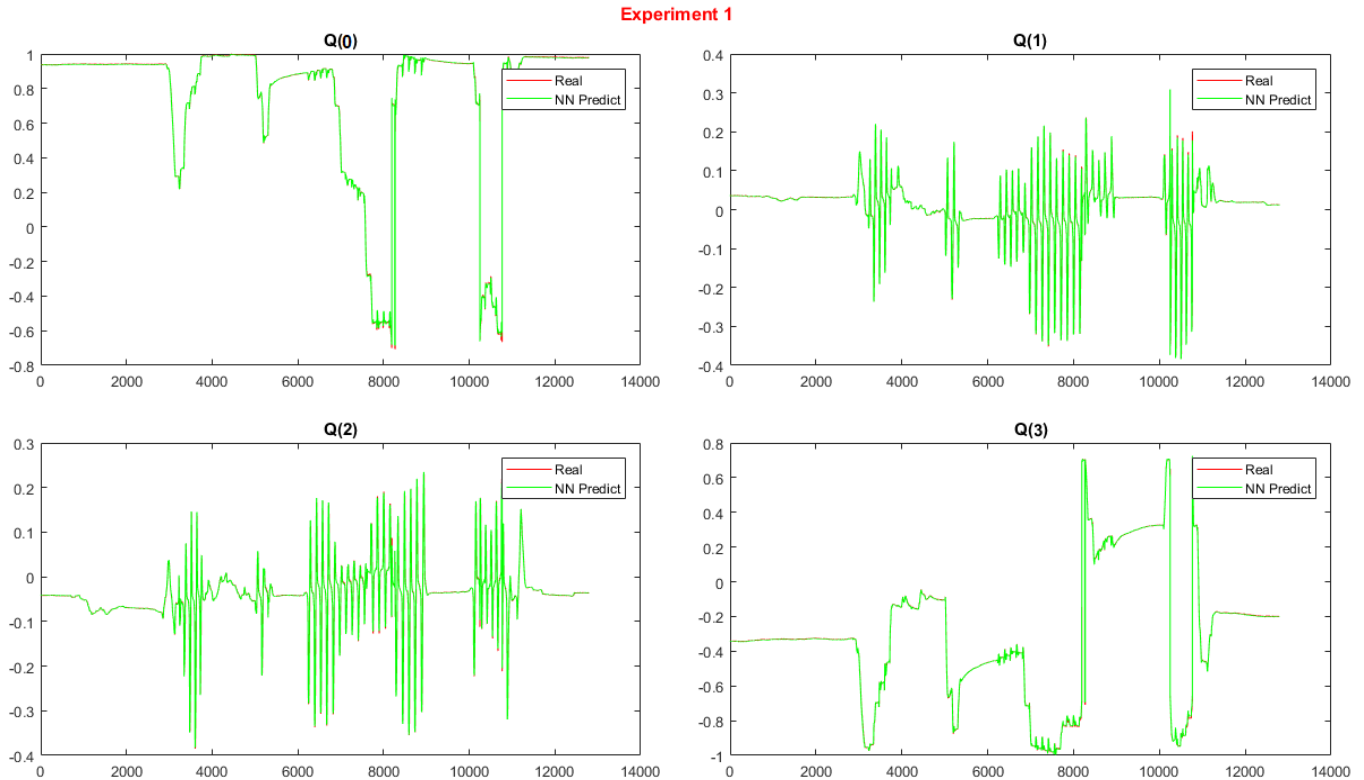


Figure 9 Training results of first ANN for $x = [q_0; q_1; q_2; q_3]$ quaternion vector

As shown in Figure 13, a particular acoustic sound calibration device was prepared to record sound from crack for different hole sizes and pressure intensity. This apparatus comprises a 20cm diameter and 3m long tube with both ends closed. Water was pumped from one end of the pipe, and the water pressure level can be adjusted between 1 and 5 bar. The water pressure intensity can be seen with the pressure gauge at the pipe inlet. In order to measure the acoustic sound signal, a wired hydrophone was placed inwardly from the other end and positioned on the opening holes to record the voices. Measured acoustic data was amplified by the preamplifier, transferred to an oscilloscope for display and recording.

Two different types of pipes (PVC and Iron Casting) were used to apply the system. Images of both applications are shown in Figure 14. In the experiment where the PVC material was used, the end cap cover could not withstand the pressure and jumped 15 meters away from the pipe. Experiments to prevent this situation did not give any results, and the experiments with PVC pipe were terminated. The experiment was carried out successfully by using the iron casting material type (Figure 14b). The sound data in the pipe were recorded for different hole sizes and pressure intensities using the RESON hydrophone. Tektronix MSO-3014 digital oscilloscope was used to record the hydrophone data. In order to measure the water pressure in the metal pipe, a

manometer, which can measure up to 10 bar, was installed. Figure 15 shows the working environment in which the prepared sound system was tested. On the left, there is a sound recording device with an oscilloscope and preamplifiers.

The centre image shows the pool and the Iron Casting sound system used for water extraction and evacuation. When the metal pipe's water pressure increased to 4.8 bar, the water was discharged from the pipe via the outlet valve.

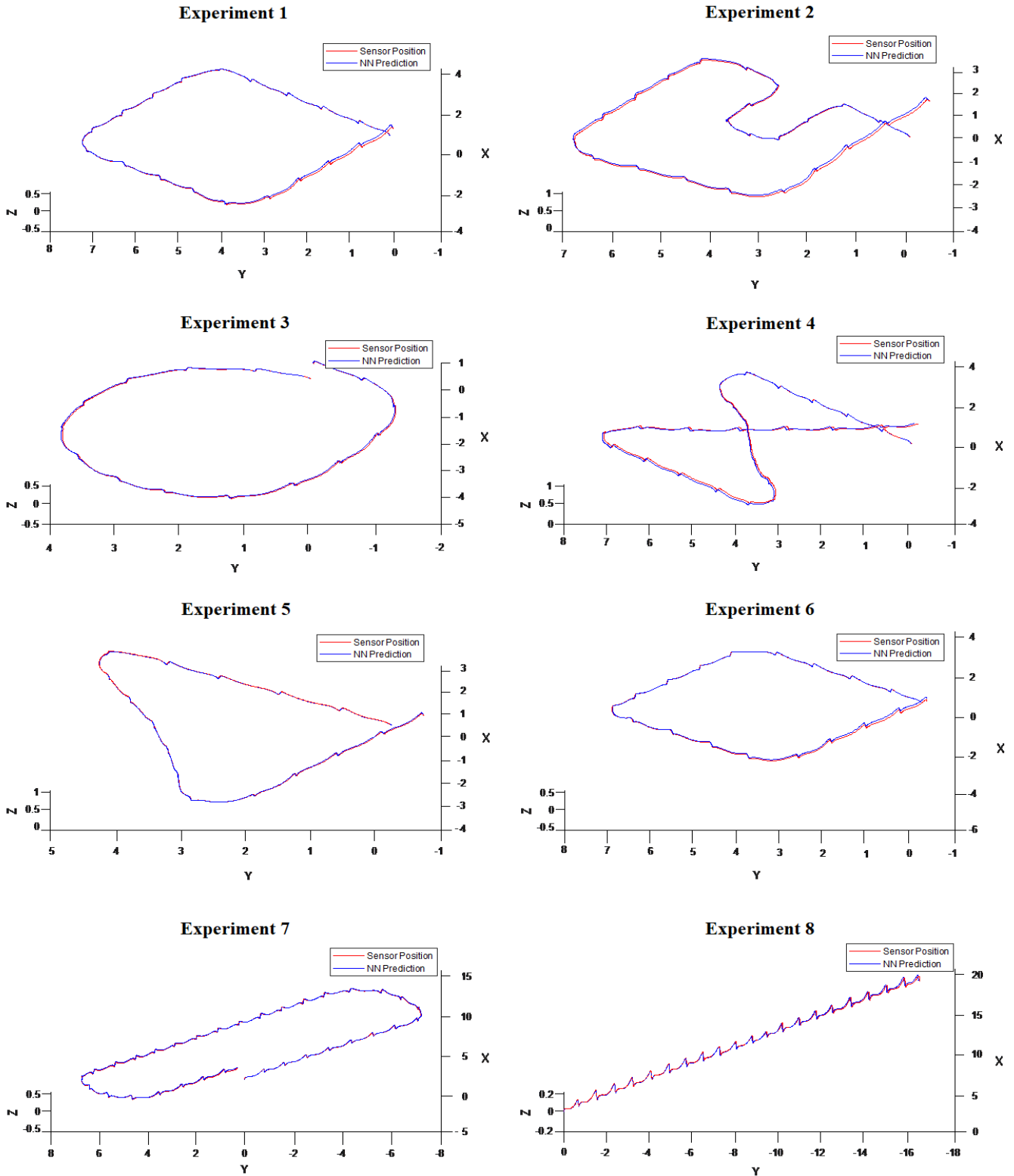


Figure 10 Estimation of navigation scenario locations by classical (red) and artificial learning method (blue).

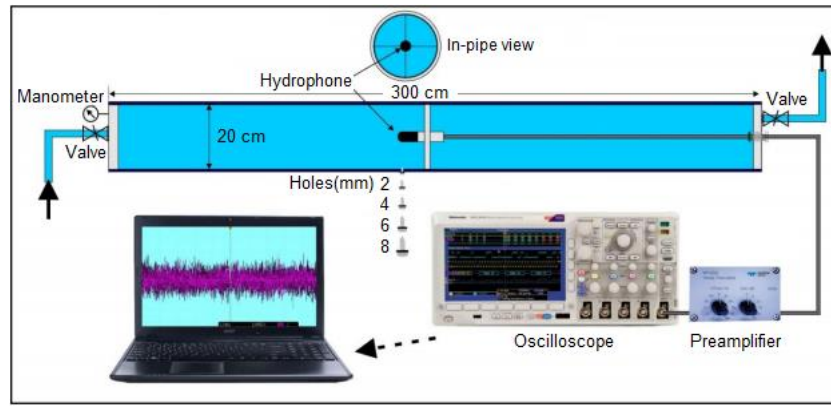


Figure 11 Sound calibration hardware.



Figure 12 Sound mechanisms (a) PVC pipe assembly (b) Iron Cast pipe assembly (c) Manometer.

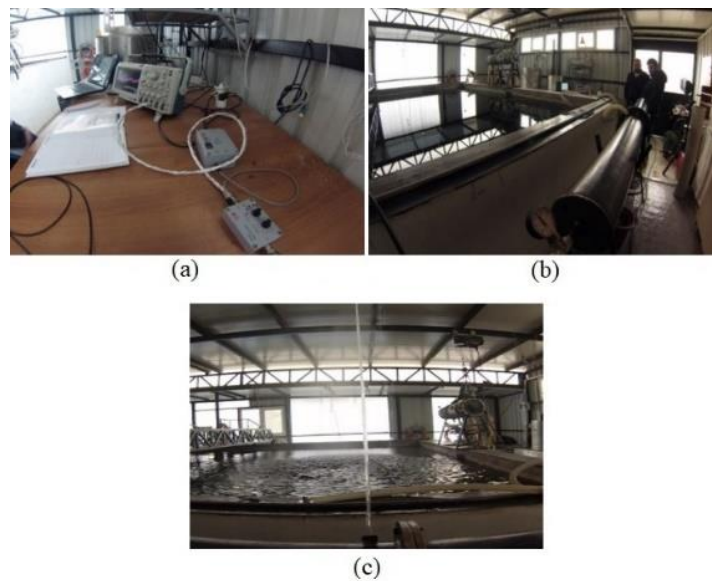


Figure 13 Experimental working environment (a) Sound recording device (b) Pool and perforated pipe (c) water jetting at 4.8bar pressure.

3.2. Measurements with Sound System

In experimental studies, the preamplifier's gain was set at 26dB, the value of the high-pass filter was set to 0.1Hz, and then measurements were performed. Each measurement was recorded numerically via the oscilloscope. The spectra in the frequency range of 0.1Hz-100kHz were visualized to see the frequency range of the sound characteristic from the crack. In order to understand the noise characteristic of the system, after the holes were closed, a pressure of 0-5bar was created in the pipe and measurements were completed (see Figure 16). Figure 17 illustrates how hole sizes and pressure intensity affect frequency and amplitude.

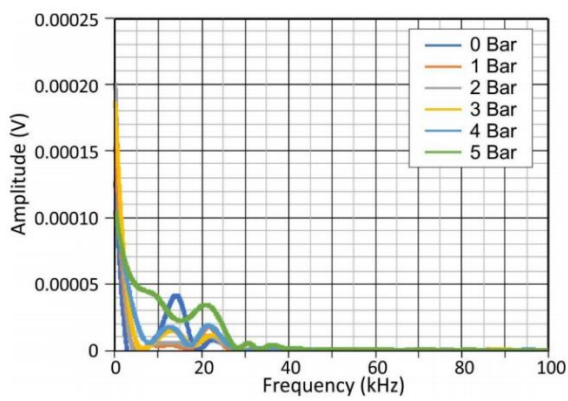


Figure 14 The noise characteristics of the system.

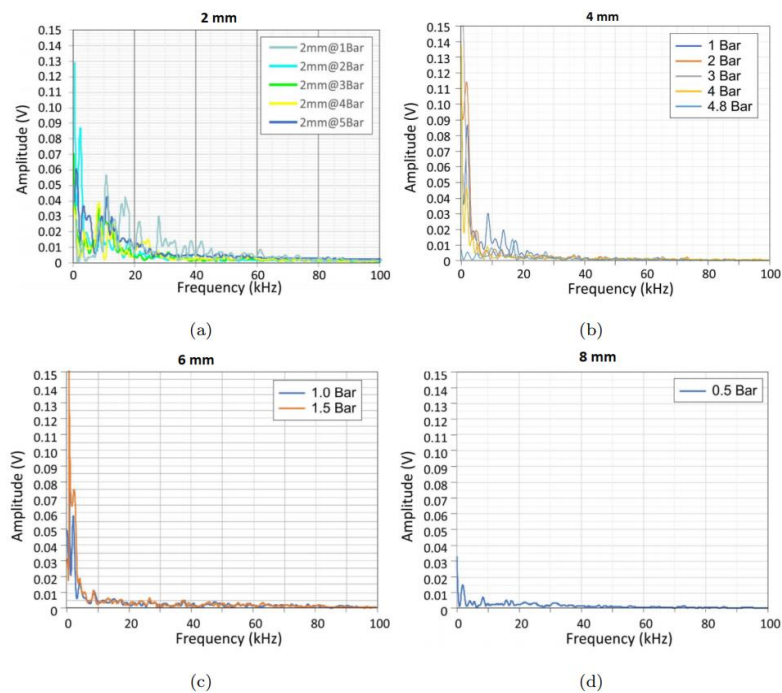


Figure 15 Effect of pressure magnitude on different hole sizes:(a)2mm; (b)4mm; (c)6mm; (d)8mm.

The following results were found after the graphs were evaluated:

- The cracked audio signal frequency was found in the 0.1Hz-40kHz band range.
- The cracked sound signal amplitude was found to be a maximum of 0.15V.
- The noise level of the system was found to be 0.0002V.
- It was seen that the oscillations were not reduced regularly as a result of the increase in pressure from 1Bar to 5Bar. This finding clearly shows that the system does not have a linear characteristic.
- It was seen that while the hole diameter increases, the acoustic signals are directed towards the low frequencies.
- It is foreseen that the same parameters can be used in the system to be designed because of the acceptable results obtained from the 26dB gain preamplifier and 0.1Hz high pass filter used during the measurements.

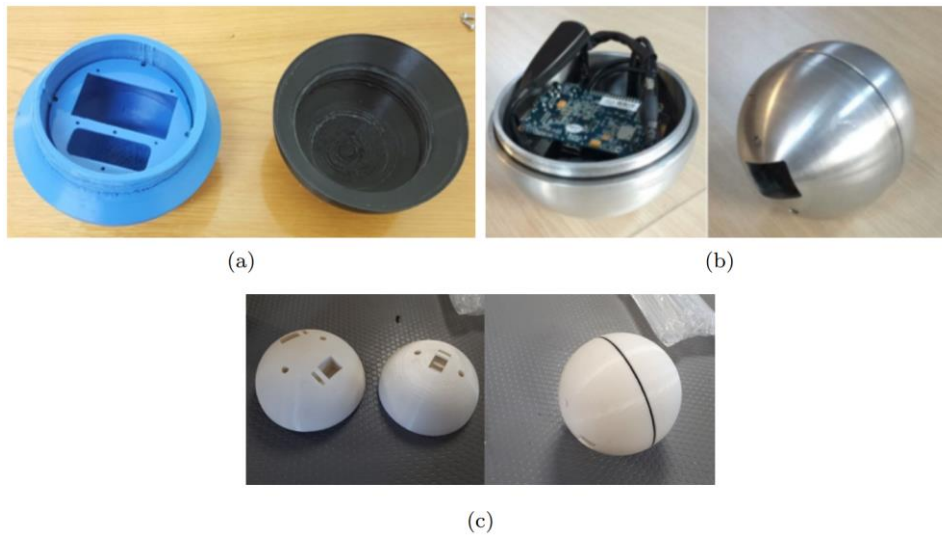


Figure 16 External sphere prototypes;(a) IMU only recording (b) IMU+single hydrophone recording, not circular;(c) IMU+three hydrophone recording, circular

4. EXTERNAL SPHERE HOUSING STUDIES

In this study, the external sphere prototyping to maintain the electronic recording device (minicomputer, IMU, hydrophone, battery) was used and enabled independent data recording. Three different external sphere prototypes were produced. The first prototype was used to register IMU sensor data in walking scenarios (see Figure 18a). This prototype was only used on the ground because of having a water-permeable structure. A second external sphere design was needed to make the work on a basis similar to the water-filled pipes. Figure 18b shows the outer sphere prototype using metal material. However, the prototype's weight and the lack of a round geometry prevented the sphere from moving at the desired speed in the pipeline. In addition, the use of a single hydrophone for voice recording prevents the recording of sound equally in all directions. A third external sphere design was needed to overcome these problems (see Figure 18c). Because the last outer sphere is not metal, it is lighter and circular. There are three different hydrophone sensor locations on the sphere, allowing equal recording of the sound frequencies

in all directions. In addition, this sphere has a waterproof structure.

5. CONCLUSION

In conclusion, a leak detection robot ball was designed to prevent water loss in distribution networks. Precise location estimation, sound frequency range discovery and external sphere studies of the ball was performed. In addition to classical studies, the artificial learning architecture was presented in the precise position estimation studies. The methods were compared using data from eight different motion scenarios. According to this, the proposed method performs online and have a 99% similar position estimation with the classical approach. Apart from classical pattern recognition and curve-fitting architectures, time-based NN architecture was applied. In the sound wave calibration step, two experimental setups, plastic and metal, were prepared. It was examined how different hole sizes (2mm-8mm) and different pressure intensity (0bar-5bar) change the sound of the crack using plastic and metal setups. Finally, a waterproof, external sphere design that uses three different hydrophones was produced.

Funding

This study was supported by The Scientific and Technological Research Council of Turkey (TUBITAK), Project Title: "Su Borularındaki Sızıntının Tespiti İçin Orta-Ölçekli Kapsül Robot Prototipinin Üretilmesi"; Project Number: 215E075.

The Declaration of Conflict of Interest/ Common Interest

No conflict of interest or common interest has been declared by the author.

The Declaration of Ethics Committee Approval

This study does not require ethics committee permission or any special permission.

The Declaration of Research and Publication Ethics

The author of the paper declare that they comply with the scientific, ethical and quotation rules of SAUJS in all processes of the paper and that they do not make any falsification on the data collected. In addition, they declare that Sakarya University Journal of Science and its editorial board have no responsibility for any ethical violations that may be encountered, and that this study has not been evaluated in any academic publication environment other than Sakarya University Journal of Science.

Authors' Contribution

The authors contributed equally to the study.

REFERENCES

- [1] R. McKenzie and C. Seago, "Assessment of real losses in potable water distribution systems: Some recent developments," in *Water Science and Technology: Water Supply*, 2005, vol. 5, no. 1, pp. 33–40.
- [2] P. Marin, B. Kingdom, and R. Liemberger, "The challenge of reducing non-revenue water (NRW) in developing countries - how the private sector can help : a look at performance-based service contracting," Dec. 2006.
- [3] S. M. Hooda, "Rajasthan Water Assessment: Potential for Private Sector Interventions," New Delhi, © World Bank, 2017.
- [4] "Infrastructure Report Card 2017." [Online]. Available: <https://www.infrastructurereportcard.org/wp-content/uploads/2017/01/Drinking-Water-Final.pdf>. [Accessed: 20-May-2021].
- [5] N. Pizzi and W. Lauer, *Water distribution operator training handbook - Fourth Edition*, 3rd ed. American Water Works Association, 2013.
- [6] D. Misiunas, "Failure monitoring and asset condition assessment in water supply systems," Sweden, 2005.
- [7] O. Hunaidi, A. Wang, M. Bracken, T. Gambino, and C. Fricke, "Acoustic methods for locating leaks in municipal water pipe networks," 2004, pp. 1–14.
- [8] A.W.W.A., *Water Audits and Loss Control Programs(M36): AWWA Manual of Practice*, 4 edition. Denver: American Waterworks Association, 2016.
- [9] S. H. Zyoud, L. G. Kaufmann, H. Shaheen, S. Samhan, and D. Fuchs-Hanusch, "A framework for water loss management in developing countries under fuzzy environment: Integration of Fuzzy AHP with Fuzzy TOPSIS," *Expert Syst. Appl.*, vol. 61, pp. 86–105, Nov. 2016.
- [10] S. Eggimann *et al.*, "The Potential of Knowing More: A Review of Data-Driven Urban Water Management," *Environmental Science and Technology*, vol. 51, no. 5. American Chemical Society, pp. 2538–2553, 07-Mar-2017.
- [11] A. Gupta and K. D. Kulat, "A Selective Literature Review on Leak Management

- Techniques for Water Distribution System,” *Water Resources Management*, vol. 32, no. 10. Springer Netherlands, pp. 3247–3269, 01-Aug-2018.
- [12] M. FIRAT, S. YILMAZ, and C. ORHAN, “Su kayıp yönetimi için temel hesaplama araçlarının geliştirilmesi ve temel su kayıp bileşenlerinin analizi,” *Gümüşhane Üniversitesi Fen Bilim. Enstitüsü Derg.*, vol. 11, no. 2, pp. 405–416, Feb. 2021.
- [13] M. Eugene, “Predictive Leakage Estimation using the Cumulative Minimum Night Flow Approach,” *Am. J. Water Resour.*, vol. 5, no. 1, pp. 1–4, Jan. 2017.
- [14] E. Farah and I. Shahrour, “Leakage Detection Using Smart Water System: Combination of Water Balance and Automated Minimum Night Flow,” *Water Resour. Manag.*, vol. 31, no. 15, pp. 4821–4833, Dec. 2017.
- [15] E. Roshani and Y. Fillion, “WDS leakage management through pressure control and pipes rehabilitation using an optimization approach,” in *Procedia Engineering*, 2014, vol. 89, pp. 21–28.
- [16] N. Fontana, M. Giugni, L. Glielmo, G. Marini, and R. Zollo, “Real-Time Control of Pressure for Leakage Reduction in Water Distribution Network: Field Experiments,” *J. Water Resour. Plan. Manag.*, vol. 144, no. 3, p. 04017096, Mar. 2018.
- [17] Y. Kleiner, B. J. Adams, and J. S. Rogers, “Water distribution network renewal planning,” vol. 15, no. 1, pp. 15–26, Jan. 2001.
- [18] E. Mann and J. Frey, “Optimized pipe renewal programs ensure cost-effective asset management,” in *Pipelines 2011: A Sound Conduit for Sharing Solutions - Proceedings of the Pipelines 2011 Conference*, 2011, pp. 44–54.
- [19] I. Moslehi and M. Jalili_Ghazizadeh, “Pressure-Pipe Breaks Relationship in Water Distribution Networks: A Statistical Analysis,” *Water Resour. Manag.*, vol. 34, no. 9, pp. 2851–2868, Jul. 2020.
- [20] A. E. Akkaya and M. F. Talu, “Extended kalman filter based IMU sensor fusion application for leakage position detection in water pipelines,” *J. Fac. Eng. Archit. Gazi Univ.*, vol. 32, no. 4, 2017.
- [21] C. Uyanik, E. Erdemir, E. Kaplanoglu, and A. Sekmen, “A deep learning approach for motion segment estimation for pipe leak detection robot,” in *Procedia Computer Science*, 2019, vol. 158, pp. 37–44.
- [22] S. Kazeminasab, V. Janfaza, M. Razavi, and M. K. Banks, “Smart Navigation for an In-pipe Robot Through Multi-phase Motion Control and Particle Filtering Method,” *CoRR*, vol. abs/2102.1, Feb. 2021.
- [23] S. Kazeminasab, R. Jafari, and M. Katherine Banks, “An LQR-assisted Control Algorithm for an Under-actuated In-pipe Robot in Water Distribution Systems,” in *Proceedings of the 36th Annual ACM Symposium on Applied Computing*, 2021.
- [24] W. Elmenreich, “Sensor Fusion in Time-Triggered Systems,” Austria, 2002.
- [25] C. Li, C. Yang, J. Wan, A. S. Annamalai, and A. Cangelosi, “Teleoperation control of Baxter robot using Kalman filter-based sensor fusion,” *Syst. Sci. Control Eng.*, vol. 5, no. 1, pp. 156–167, Jan. 2017.
- [26] T. Zhang and Y. Liao, “Attitude measure system based on extended Kalman filter for multi-rotors,” *Comput. Electron. Agric.*, vol. 134, pp. 19–26, Mar. 2017.
- [27] Y. Liu, S. Gong, and Y. Lu, “Estimation of inertial/magnetic sensor orientation for human-motion-capture system,” 2017, pp. 175–179.

- [28] S. Qiu, Z. Wang, H. Zhao, K. Qin, Z. Li, and H. Hu, "Inertial/magnetic sensors based pedestrian dead reckoning by means of multi-sensor fusion," *Inf. Fusion*, vol. 39, pp. 108–119, Jan. 2018.
- [29] R. Kalman, "A New Approach to Linear Filtering and Prediction Problems," *Trans. ASME – J. Basic Eng.*, no. 82 (Series D), pp. 35–45, 1960.
- [30] M. S. Grewal and A. P. Andrews, *Kalman Filtering: Theory and Practice Using MATLAB*, 3rd editio. Wiley-IEEE, 2008.
- [31] G. Bishop and G. Welch, "An Introduction to the Kalman Filter." University of North Carolina SIGGRAPH 2001 course notes. ACM Inc., North Carolina, 2001.
- [32] S. O. H. Madgwick, A. J. L. Harrison, and R. Vaidyanathan, "Estimation of IMU and MARG orientation using a gradient descent algorithm," 2011, pp. 1–7.
- [33] N. Trawny and S. I. Roumeliotis, "Indirect Kalman Filter for 3D Attitude Estimation A Tutorial for Quaternion Algebra Multiple Autonomous Robotic Systems Laboratory, Technical report," Mar. 2005.
- [34] W. H. K. de Vries, H. E. J. Veeger, C. T. M. Baten, and F. C. T. van der Helm, "Magnetic distortion in motion labs, implications for validating inertial magnetic sensors," *Gait Posture*, vol. 29, no. 4, pp. 535–541, Jun. 2009.
- [35] C. Wang, X. Qu, X. Zhang, W. Zhu, and G. Fang, "A Fast Calibration Method for Magnetometer Array and the Application of Ferromagnetic Target Localization," *IEEE Trans. Instrum. Meas.*, vol. 66, no. 7, pp. 1743–1750, Jul. 2017.
- [36] A. M. Sabatini, "Quaternion-based extended Kalman filter for determining orientation by inertial and magnetic sensing," *IEEE Trans. Biomed. Eng.*, vol. 53, no. 7, pp. 1346–1356, Jul. 2006.
- [37] Ruoyu Zhi, "A Drift Eliminated Attitude & Position Estimation Algorithm In 3D," The University of Vermont, 2016.